Journal of Structural Geology 32 (2010) 1834–1849

Contents lists available at ScienceDirect

Journal of Structural Geology

journal homepage: www.elsevier.com/locate/jsg

Clay smear in normal fault zones – The effect of multilayers and clay cementation in water-saturated model experiments

J. Schmatz [a,*], P.J. Vrolijk [b], J.L. Urai [a]

[a] Structural Geology, Tectonics and Geomechanics, Geological Institute, RWTH Aachen University, Lochnerstrasse 4-20, 52056 Aachen, Germany
[b] ExxonMobil Upstream Research Co., P.O. Box 2189, Houston, TX, USA

ARTICLE INFO

Article history:
Received 29 April 2009
Received in revised form
10 December 2009
Accepted 13 December 2009
Available online 4 January 2010

Keywords:
Clay smear
Fault seal
Mechanical layering
Competence contrast
Experimental model

ABSTRACT

We studied the evolution of fault zones in water-saturated model experiments consisting of sand and clay layers above a normal fault dipping 70° in a stiff basal layer. The model is bounded below by a rigid metal basement with a pre-cut 70° fault and above by a metal plate, also with a 70° cut, aligned in the same plane as the basement fault. Quantitative analysis of particle displacements was undertaken with PIV (Particle Image Velocimetry) software. In these models, the structure of initial localized deformation evolves into a kinematically favorable fault zone. This evolution, which produces releasing or restraining relays across the clay layer, has a major role in controlling fault-zone structure. We show that a high competence contrast between sand and clay leads to a more complex fault zone due to the formation of secondary shear zones and segmentation-induced fault lenses. A high competence contrast also promotes a more complex temporal evolution of those shear zones. Weak clay layers are preferentially enriched in fault zones, whereas strong, brittle clay initially fractures and forms clay boudins that rotate in the deforming sand. With progressive deformation these boudins are abraded and transformed into a soft-clay gouge. Thin, weak clays deform continuously over large displacements, and the volume of clay-rich gouge increases as sand mixes into clay at the margins of the shear zone. Thus, we observe a wide range of fault zone and fault gouge evolution by adjusting the mechanical properties of the clay. Further physical insights into fault processes like those reached here may yield predictive models of fault-zone evolution that will transcend empirical methods (e.g., shale-gouge ratio, SGR).

1. Introduction

Fault networks have a major effect on hydromechanical processes in sedimentary basins. We have a basic understanding of the basic physical processes of fault sealing, but the complex geometries and many feedback processes make quantitative prediction difficult. Fault zones have been widely investigated in field studies, experimental models and numerical simulations to better understand their transport and sealing properties (e.g., Weber et al., 1978; Lehner and Pilaar, 1991, 1997; Antonellini et al., 1994; Fulljames et al., 1997; Clausen and Gabrielsen, 2002; James et al., 2004; Egholm et al., 2008; Mair and Abe, 2008; Urai et al., 2008).

Much of the research on faults in sand–clay sequences is focused on predicting the amount of clay incorporated into the fault gouge, commonly called clay smear. Clay smear, a loosely defined term used in hydrocarbon geology, describes the processes in which clay from the wall rock is incorporated in a fault zone (Yielding et al., 1997). In subsurface studies, numerous statistical algorithms are used for clay smear analysis: clay-smear potential, shale-smear factor and shale-gouge ratio (Lindsay et al., 1993; Fristad et al., 1997; Fulljames et al., 1997; Yielding et al., 1997; Yielding, 2002). Most of these methods are based on the assumption that fault gouge consists of a reworked equivalent of the wall rocks offset by a fault (Holland et al., 2006) without the addition or removal of material (van Gent et al., in press). Because this method averages over the lithologic interval offset by the fault, it fails to accurately predict the spatial distribution of clay along the fault plane. In addition, the mechanical properties of the rocks in the wall rock and fault zone are neglected. Clearly, a better understanding of the processes involved during faulting would improve the quality of fault-seal predictions.

When a segmented normal fault cuts heterogeneously layered sequences with competence contrast, (e.g., clay and sand), the fault develops a steeper dip in layers with a higher friction angle and a shallower dip in layers with a lower friction angle (Peacock and Sanderson, 1992). This results in vertically segmented faults with steps at lithologic/competency boundaries (Childs et al., 1996).

* Corresponding author. Fax: +49 80 92358.
E-mail addresses: j.schmatz@ged.rwth-aachen.de (J. Schmatz), peter.vrolijk@exxonmobil.com (P.J. Vrolijk), j.urai@ged.rwth-aachen.de (J.L. Urai).

0191-8141/$ – see front matter © 2009 Elsevier Ltd. All rights reserved.
doi:10.1016/j.jsg.2009.12.006

Other authors (e.g., Lehner and Pilaar, 1997; Van der Zee et al., 2003) postulated that "clay injection" is able to enrich the fault with clay over the amount expected by lithologic offset. The clay injection mechanism proposed by Lehner and Pilaar (1997) contains two essential elements: (1) a pull-apart structure forms when the fault crosses a clay layer. (2) The clay bed is injected into this pull-apart structure and subsequently sheared to form a thick clay gouge. The injection process requires significantly weaker clay than the surrounding sand layers (Van der Zee et al., 2003). van Gent et al. (in press) describe a fundamentally different process of clay enrichment, which involves the vertical transport of clay along dilatant fractures in brittle carbonates.

Experiments by Sperrevik et al. (2000) and Clausen and Gabrielsen (2002) showed a strong dependency of clay smear on the mechanical properties of the materials. They used a ring-shear apparatus to deform clay and sand layers to high strains at variable normal stresses. They observed pronounced clay smear with increasing stresses and decreasing clay strength. In a preliminary set of experiments of layered sand–clay sequences, Schmatz et al. (2010) varied the clay-layer proportions, clay-layer thickness and spacing, and clay composition; normal faulting created continuous smear in weak, under-consolidated clay; in contrast, a strong, over-consolidated clay first deforms in a brittle mode and then sometimes becomes reworked to form a soft-clay gouge. Here we present the results of water-saturated experiments with the added boundary condition of a strong top layer containing a pre-cut fault in a kinematically favorable orientation to the basement fault, and investigate the effect of different multilayer configurations and clay cementation on the structure of the evolving fault zone.

In experiments with a free top surface, deformation is less localized at the top of the model (Fig. 1). Pilot experiments (Schmatz et al., 2010) show that a top plate and basement fault acting together form two precursor faults: one initiating at the tip of the basement fault, and one at the tip of the fault in the top plate (cf. quadshear, Welch et al., 2009). With progressive deformation they link up across the model to form a kinematically favored zone of deformation.

2. Methods

2.1. Setup

A sandbox was constructed to deform water-saturated, layered ($40 \times 20 \times 20$ cm) (width/height/depth) sand–clay models (Fig. 2). In this series of experiments, the boundary conditions were chosen to simulate a series of weaker layers sandwiched between two strong and stiff layers cut by two co-planar faults dipping 70° (see also Mandl, 2000; Van der Zee, 2002; Ferrill and Morris, 2003; Adam et al., 2005). Water-saturated models allowed the deformation of wet clay and cohesionless sand together in one model (Schmatz et al., 2010). The basement fault moved at 40 mm/h to a maximum offset of 60 mm. The models were run between two glass plates lubricated to minimize edge effects. At this deformation rate, the thick clay layers were sheared under undrained conditions, whereas pore pressures likely remained hydrostatic inside the fine-grained sand. The resulting material properties were characterized by a series of standard geotechnical measurements. Full details of the methods for a free-surface boundary condition are given in Schmatz et al. (2010). Here we summarize the most important aspects and procedures that result from additional boundary conditions and experiment designs.

2.2. Boundary conditions

We used 2 cm thick aluminum ($\rho = 2400$ kg m^{-3}) top plates, pre-cut at the same 70° angle as the basement fault, placed on top

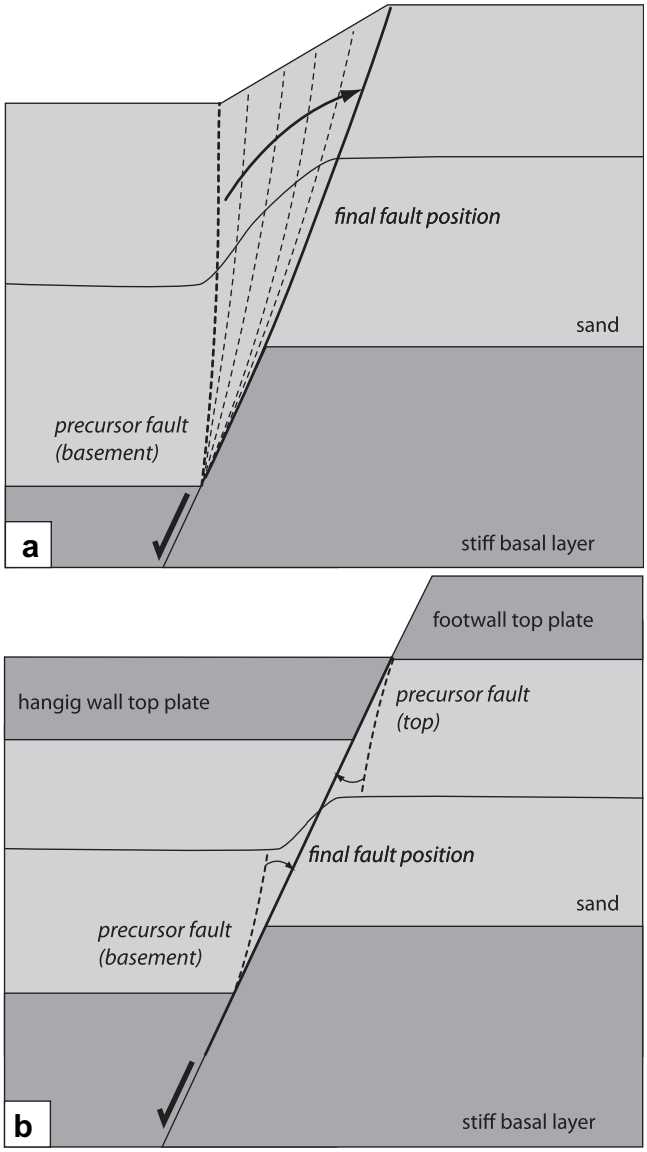

Fig. 1. (a) Sketch showing boundary conditions and fault evolution in an experiment with a free surface. The steep precursor fault is shown with a dashed line. The fault rotates into its kinematically favored position (bold line). Compare to Schmatz et al. (2010). (b) Sketch showing boundary conditions and fault evolution in an experiment with rigid top plates. Two precursor faults develop, initiating at the tip of the faults in the basement and top plates. With progressive deformation, the zone of deformation migrates into the center of the model (bold line).

of the models and aligned (co-planar) with the basement fault (Fig. 1). The stiff base plate acts as a rigid guide compared to the sediment, and the top plates rotate and move but without bending. Approximately 40 experiments were run using variable clay strengths and number and thicknesses of the clay layers to investigate fault-zone processes. The experiments were recorded with time-lapse photographs (Schmatz et al., 2010) with constant time interval and resolution, and are presented throughout the paper cropped to the same section.

2.3. Sand

We used the same washed, well-sorted quartz sand with a grain size of 0.1–0.4 mm as in Schmatz et al. (2010), with colored marker horizons. The grain size range results in sand packing classified as medium-dense; thus, the sand yields at a distinct peak shear

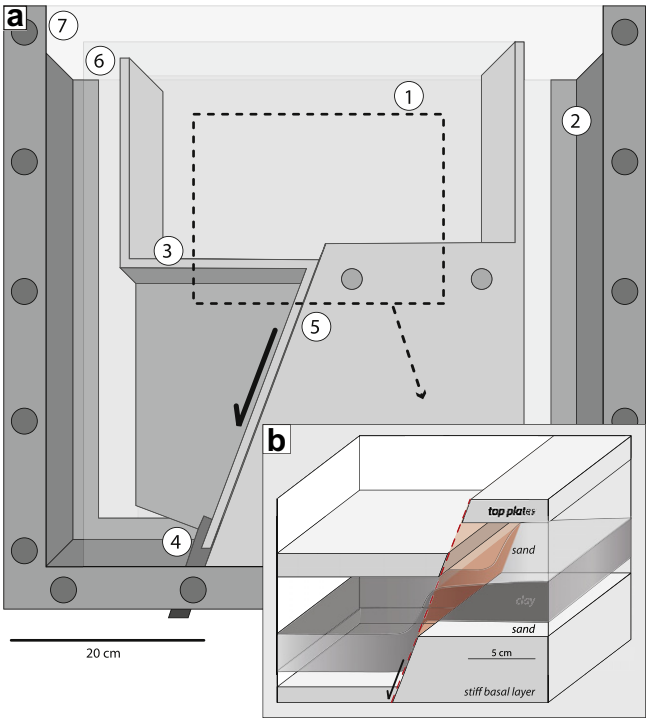

Fig. 2. (a) Sketch of the underwater experimental apparatus with: 1) water-saturated apparatus (inside), 2) waterproof container (outside), 3) rigid basement bottom with drain perforation, 4) motor-driven fault offset, 5) basement fault dipping 70°, 6) movable glass plate (inside), 7) movable glass plate (outside). (b) Sketch of setup showing alternating layers of sand and clay overlying stiff basal block, covered with pre-cut aluminum top plates. Red area indicates kinematically favored position of the fault. (For interpretation of the references to colour in this figure legend, the reader is referred to the web version of this article.)

strength and forms a localized shear band in the experimental model.

2.4. Clay

The clay is a quartz (46.8%)–kaolinite (42.0%) mixture with water contents of ~30, 40 and 50 wt.%, representing over-consolidated (firm), normal-consolidated (normal) and under-consolidated (soft) clay, respectively. Direct shear tests indicate a ten times higher undrained shear strength for firm clay than for soft clay (Schmatz et al., 2010). In some experiments, small amounts (0.25–10 wt.%) of Portland cement were added to the soft clay. The cement hardened (while water-saturated) the clay in ~17 h. Geotechnical measurements show undrained shear strength with a linear increase from 2.6 kPa (1.0 wt.% cement) to 27 kPa (5.0 wt.% cement). By comparison, firm but uncemented clay has a shear strength of ~2.4 kPa. To ensure that the cemented clay was completely cured, most of the models were left overnight before starting the deformation experiment.

2.5. Particle image velocimetry (PIV)

Time-lapse series of high-resolution digital images were processed into movies and analyzed using PIV (e.g., Wolf et al., 2003; Adam et al., 2005; Steingart and Evans, 2005; Holland et al., 2006; van Gent et al., in press). The PIV analysis documents displacements of a granular structure on the particle scale and gives detailed velocity fields. The resolution is given by an interrogation window size of 128 × 128 pixels decreasing to a window of 32 × 32 pixels with an overlap of 75% producing a final window size of 8 × 8 pixels, which corresponds to approximately 16 sand grains in our experiments (Adam et al., 2005; Schmatz et al., 2010). Movies of all experiments are available at www.ged.rwth-aachen.de.

3. Experimental results

In this study we undertook nine systematic experimental series. Parameters studied include: clay strength, layer thickness, and the number of layers. To allow comparison with experiments without top plates, we repeated a number of earlier experiments both with and without the top plate. The full series of experiments is summarized in Table 1. Here we describe a number of these in detail (Figs. 3–16). To check the reproducibility of the experiments, one of the experiments presented here (R-2-s-tp, Fig. 7, Table 1) was repeated four times under identical conditions. We reproduce many first-order fault structures in these repeat experiments, but sometimes small variations arise.

3.1. Effect of top plates

Counterclockwise rotation of the hanging wall top plate up to 1.8° was observed in most of the experiments. Measurements of rotation show no correlation to the clay setup, clay type or layer thickness.

3.1.1. Sand only

Our reference experiment is a water-saturated, sand-only model (Fig. 3, Table 1, experiment P-1) with a base area of 40 × 20 cm and 15 cm high, with free surface, comparable to the boundary condition used in Horsfield (1977) and also discussed in Adam et al. (2005). Initial displacement along the basement fault creates a 'precursor' fault (Mandl, 2000) which migrates through the material into a kinematically favorable position forming a triangular shear zone (e.g., Erslev, 1991; Zehnder and Allmendinger, 2000; Cardozo et al., 2003; Fig. 3a and b). PIV visualization of the incremental strain field ϵ_{yx} (Fig. 3b) shows the migration of localization through the material and formation of a stable planar deformation zone at a displacement of ~14°mm. Adding the pre-cut aluminum plates produces significantly different results (Fig. 4, Table 1, experiment P-2-tp). A precursor fault initiates from the basement fault tip, dipping at approximately 45° in the direction of the hanging wall. Almost immediately after 2 mm displacement on the basement fault, deformation is also localized at the base of the fault between the top plates, propagating downwards. With progressive deformation these two zones interact, the precursor fault becomes inactive, and deformation is localized in a stable, planar deformation zone in the plane of the basement fault. Localization is thus much more rapid than in the experiment with a free top surface (displacement of ~7°mm).

3.1.2. Sand and clay

Adding a 30 mm thick layer of firm clay to the model (Fig. 5, Table 1, experiment N-9-f) has a major impact on the fault-zone evolution. The experiment with a free surface is comparable to Figs. 9 and 11 of Schmatz et al. (2010). Here the fault-zone evolution is complex. The steep precursor fault fails to propagate across the clay layer, which instead deforms by bending. Fractures initiate at the clay–sand interface at locations of high curvature and extension. With increasing deformation the layer breaks into fragments of various sizes which then rotate and become reworked into a ductile clay gouge. The flow of sand grains along clay asperities is associated with asperity abrasion and mixing of sand and clay. Secondary faults propagate from fractures in the clay across the sand. A stable, distinct planar fault plane fails to form for offset >30 mm (Fig. 5b).

Table 1
Overview of experiment series.

Series	New ID	# Clay layers	Thickness	Layer setup (clay)	Clay type	Top plates	# Images	Velocity [mm/min]	Water content [%]	Hardening [h]	Cement [wt.%]	Figure	SGR diagram
Adam et al., 2005	P-1	0	–	150	–	–	133	0.7				4	
1) Sand only	P-2-tp	0	–	140	–	+	133	0.4	–			5, 19	
	P-3-tp	0	–	140	–	+		0.4					
2) Changing two	S-1-s	1	10	5/10/140	Soft	–	224	0.2	52				2
parameters:	S-2-s	1	3	5/3/140	Soft	–	268	0.2	52				19
clay strength and layer	S-3-f	1	3	5/10/140	Firm	–	276	0.2	27				
thickness	S-4-n	1	30	5/30/140	Normal	–	290	0.2	44				21
	S-5-n	1	10	5/10/140	Normal	–	300	0.2	40				23
	S-6-n	1	3	5/3/140	Normal	–	298	0.2	44				24
	S-7-s	1	30	10/30/140	Soft	–	310	0.2	50				9
Schmatz et al., 2010	S-8-f	1	30	5/30/140	Firm	–	296	0.2	28				34
	S-9-f	1	3	5/3/140	Firm	–	302	0.2	28				31
3) Changing four	N-1-s-tp	2	10	55/10/10/10/55	Soft	+	181	0.4	52				3
parameters:	N-2-s-tp	1	30	55/30/55	Soft	+	183	0.4	52			12, 19	5
clay strength, layer	N-3-s-tp	1	30	30	Soft	+	185	0.4	52				13
thickness,	N-4-n-tp	1	3	3	Normal	+	179	0.4	48				25
number of layers, layer	N-5-s-tp	1	3	3	Soft	+	146	0.4	52				17
orientation	N-6-s-tp	1	3	60/3/77	Soft	+	193	0.4	53				16
	N-7-s-tp	2	3	50/3/6/3/78	Soft	+	182	0.4	52				10
	N-8-f-tp	1	30	50/30/60	Firm	+	186	0.4	37			7	28
	N-9-f-	1	30	50/30/60	Firm	–	189	0.4	34			6	29
	N-10-n-tp	2	3	50/3/6/3/78	Normal	+	191	0.4	l45/u47				20
	N-11-n-tp	1	10	50/10/80	Normal	+	191	0.4	44				22
4) Changing clay layer	D-1-s-tp	2	3	40/3/30/3/64	Soft	+	187	0.4	53				8
distance	D-2-s-tp	2	3	40/3/40/3/54	Soft	+	215	0.4	53				6
	D-3-s-tp	2	3	40/3/50/3/44	Soft	+	203	0.4	53				18
5) Properties of cement	C1-1-s-tp	1	2	60/2/78	Soft	+	195	0.4	50	72	10		
	C1-2-s-tp	1	3	60/3/77	Soft	+	100	0.4	53	72	1		35
	C1-3-s-tp	1	3	60/3/77	Soft	+	158	0.4	52	72	5		
	C1-4-s-tp	1	5	60/5/75	Soft	+	181	0.4	52	48	10		
	C1-5-s-tp	1	3	60/3/77	Soft	+	126	0.4	51	22	10		
	C1-6-s-tp	1	3	60/3/77	Soft	+	157	0.4	53	2	10	10, 16	33
6) Reproduction	R-1-s-tp	2	3	40/3/40/3/54	Soft	+	184	0.4	55				11
	R-2-s-tp	2	3	40/3/40/3/54	Soft	+	181	0.4	52			8	7
	R-3-s-tp	2	3	40/3/40/3/54	Soft	+	180	0.4	50				12
	R-4-s-tp	2	3	40/3/40/3/54	Soft	+	191	0.4	51				14
	R-5-s-tp	2	3	40/3/40/3/54	Soft	+	189	0.4	53				15
7) Cement content	C2-1-s-tp	1	3	50/3/87	Soft	+	175	0.4	48	22	1		36
	C2-2-s-tp	2	3	50/3/50/3/34	Soft	+	173	0.4	49	23	1		32
	C2-3-s-tp	2	3	50/3/50/3/34	Soft	+	183	0.4	49	22	2	11	38
	C2-4-s-tp	2	3	50/3/50/3/34	Soft	+	184	0.4	49	22	0	9	27
	C2-5-s-tp	2	3	50/3/50/3/35	Soft	+	178	0.4	48	22	2		37
	C2-6-s-tp	2	3	50/3/50/3/34	Soft	+	188	0.4	50	24	0		26
8) Multilayer	M-1-s-tp	4	8	30/8/12/8/12/8/ 12/8/30	Soft	+	186	0.4	44			13, 17	4
	M-2-s-tp	4	Various	35/20/10/3/10/ 20/10/2/40	Soft	+	185	0.4	50			14	1
9) Clay		2	50	20/50/5/50/40	Soft	–	163	0.4	48				
10) Others	K-1-f-tp	1	3	60/3/77	Firm	+	178	0.4	37				30
	K-2-f-tp	1	3	50/3/87	Firm	+	133	0.4	34				
	K-3-f-tp	1	3	80/3/57	Firm	+	162	0.4	32				

In the same experiment with pre-cut top plates, both fault-zone geometry and clay-gouge evolution are markedly different (same vertical stress at the top of the clay layer; Fig. 6, Table 1, experiment N-8-f-tp). Analogous to the experiment with sand only and top plates, a precursor fault with a curvature towards the hanging wall initiates at the basement fault tip, followed by a second fault that initiates at the tip of the fault in the top plates and propagates downwards. Bending and macroscopic brittle failure are absent. The two fault segments link up across the clay layer and are progressively straightened. At a displacement of 10 mm, a nearly planar fault forms with a continuous, ~2 mm thick clay gouge.

3.2. Effect of clay strength

3.2.1. Low competence contrast

Experiment R-2-s-tp contains a 40 mm thick sand layer between two thin layers of soft clay (Fig. 7, Table 1); the clay beds compact into normal clay before the experiment ends (Schmatz et al., 2010). The competence contrast between sand and clay is thus low. The first fault initiates at the basement fault tip, followed by a second fault initiating at the fault tip at the top plates. Below the lower clay layer, the lower fault branched, with the branch on the footwall side propagating through the clay. At the upper clay layer, there was a mismatch between the two deformation bands arriving from below and above, and the fault zone was initially segmented. The final, kinematically favored fault zone thus has a number of inactive branches and is wider at the level of the clay layers with continuous clay smear between the fault strands (Fig. 7b; cf. Fig. 3b of Van der Zee et al., 2003).

Experiment C2-4-s-tp (Fig. 8, Table 1) has a similar initial stratigraphy as the one described above, but the sand between the two clay layers is 50 mm thick. To increase the competence contrast slightly, 0.25 wt.% Portland cement was added to the soft-clay mixture (this increased the strength only slightly from 0.2 kPa for

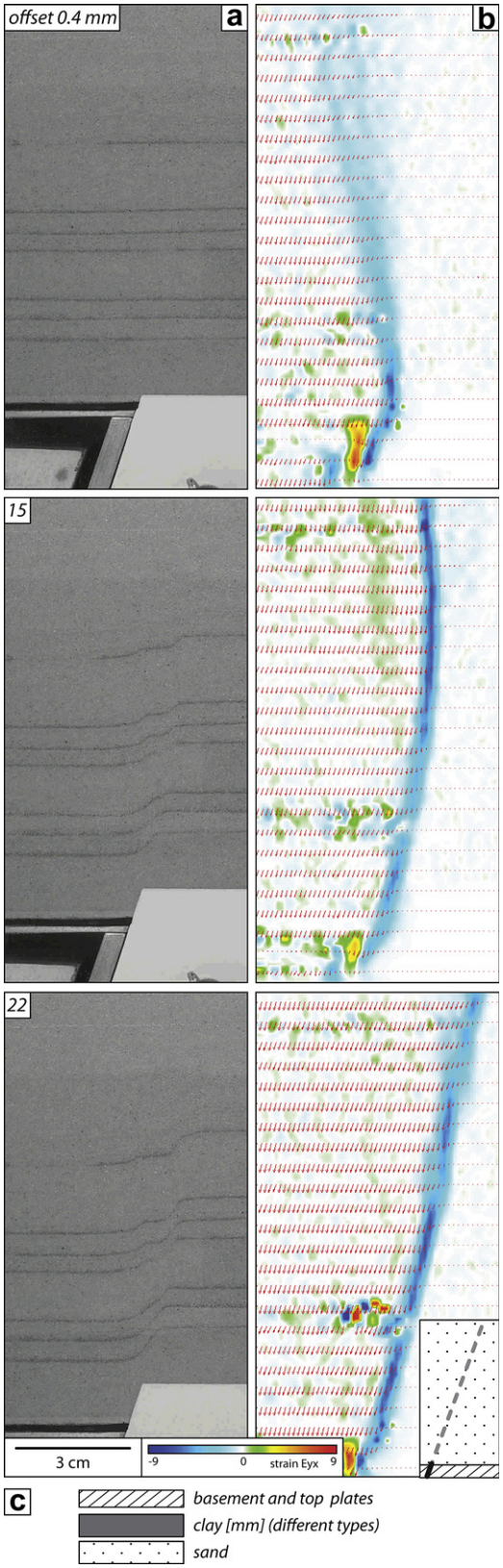

Fig. 3. (a) Image sequence showing experiment P-1 with 150 mm thick sand layer and free top surface (see inset). The three stages record offset along the basement fault of 0.4, 15, and 22 mm. (b) Image sequence showing the corresponding PIV overlay to the image sequence in (a) with the velocity vector field displayed in the foreground and the contour plot of incremental strain ϵ_{xy} in the background. Modified from Adam et al. (2005). (c) Legend for insets in Figs. 3–18.

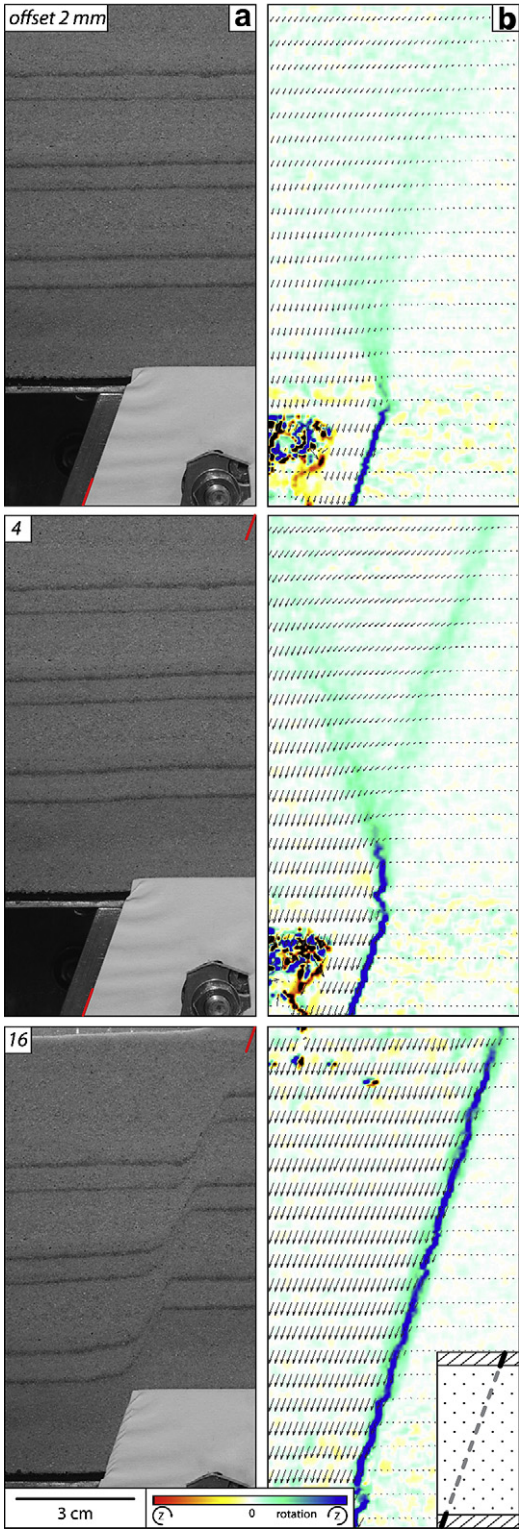

Fig. 4. (a) Image sequence showing experiment P-2-tp with a 140 mm thick sand package and top plates (see inset). Fault offset is 2, 4, and 16 mm. Red lines indicate location of rigid blocks at bottom and top. (b) Image sequence showing the corresponding PIV overlay to image sequence in (a) with the velocity vector field in the foreground and a contour plot of the z-component of the incremental rotation field in the background. (For interpretation of the references to colour in this figure legend, the reader is referred to the web version of this article.)

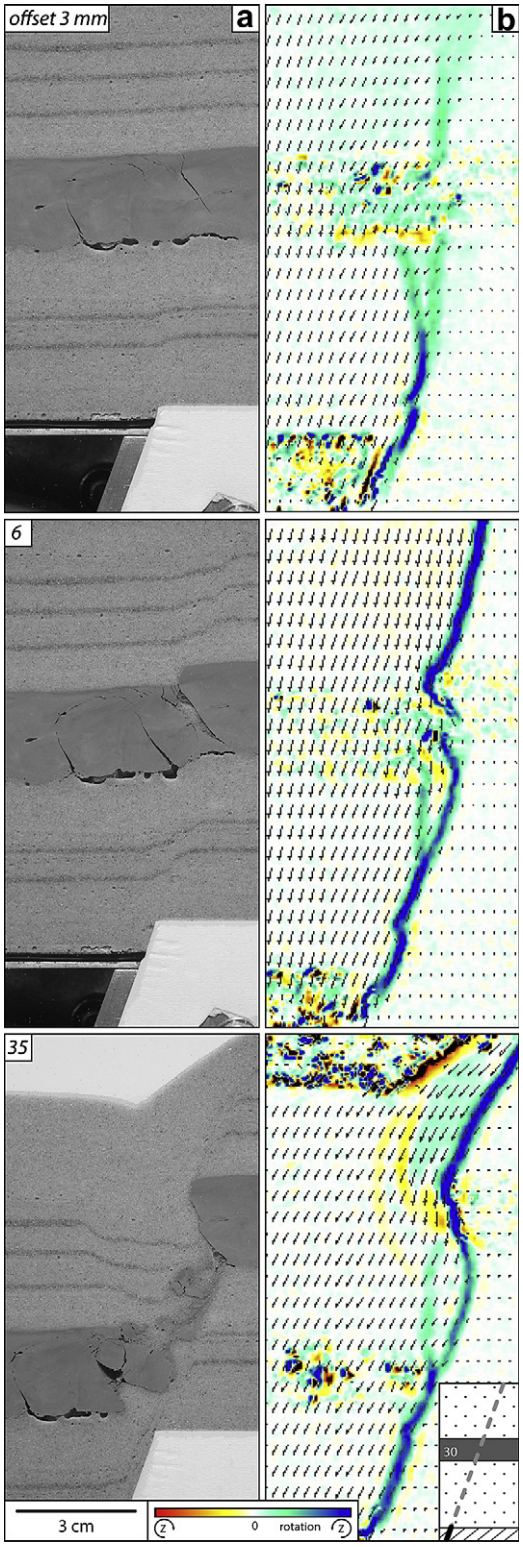

Fig. 5. (a) Image sequence showing experiment N-9-f with a 30 mm thick firm clay layer in the center and a free top surface (see inset). Basement fault offset is 3, 6, and 35 mm. (b) Image sequence showing the corresponding PIV overlay to image sequence (a) with the velocity vector field in the foreground and a contour plot of the z-component of the incremental rotation field in the background.

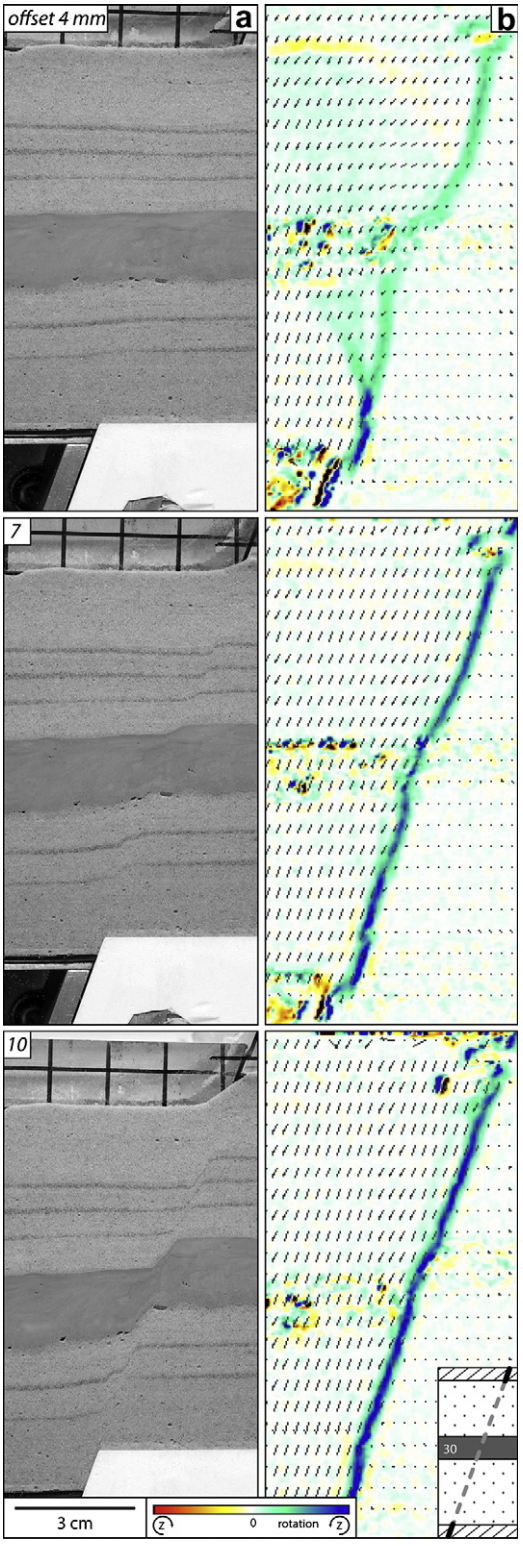

Fig. 6. (a) Image sequence showing experiment N-8-f-tp with a 30 mm thick firm clay layer in the center of the model and top plates (see inset). Basement fault offset is 4, 7 and 10 mm. (b) Image sequence showing the corresponding PIV overlay to image sequence in (a) with the velocity vector field in the foreground and a contour plot of the z-component of the incremental rotation field in the background.

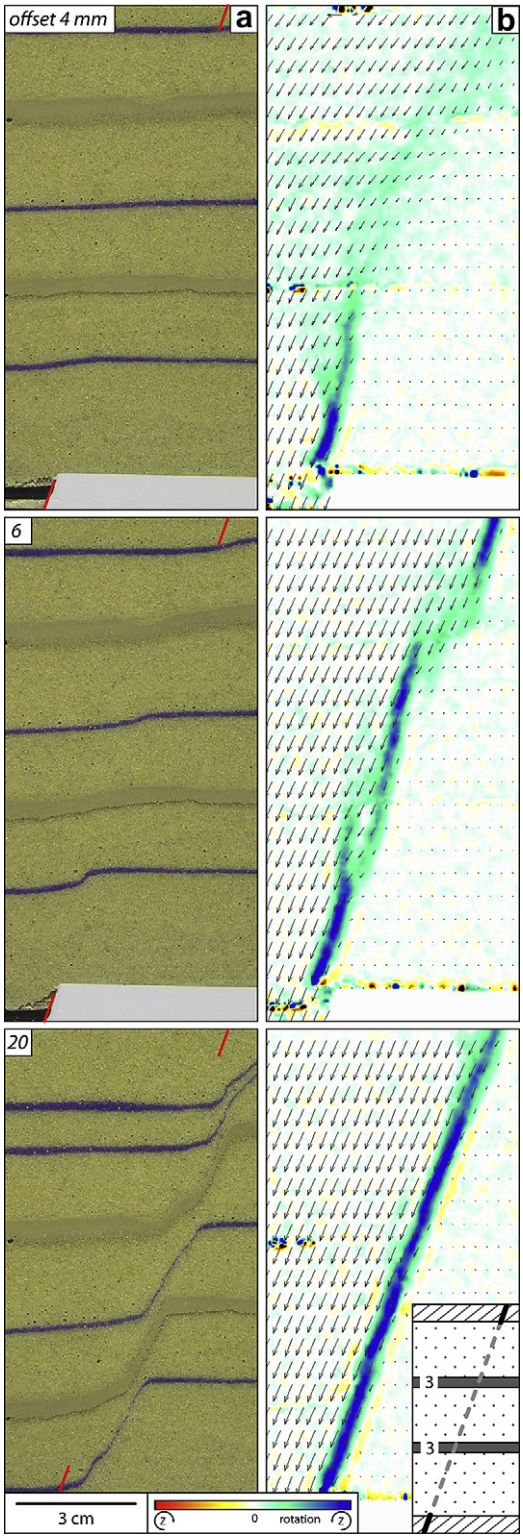

Fig. 7. (a) Image sequence showing experiment R-2-s-tp with two 3 mm thick soft-clay layers and top plates (see inset). Basement fault offset is 4, 6 and 20 mm. Red lines indicate location of rigid blocks at bottom and top. (b) Image sequence showing the corresponding PIV overlay to the image sequence in (a) with the velocity vector field in the foreground and a contour plot of the z-component of the incremental rotation field in the background. (For interpretation of the references to colour in this figure legend, the reader is referred to the web version of this article.)

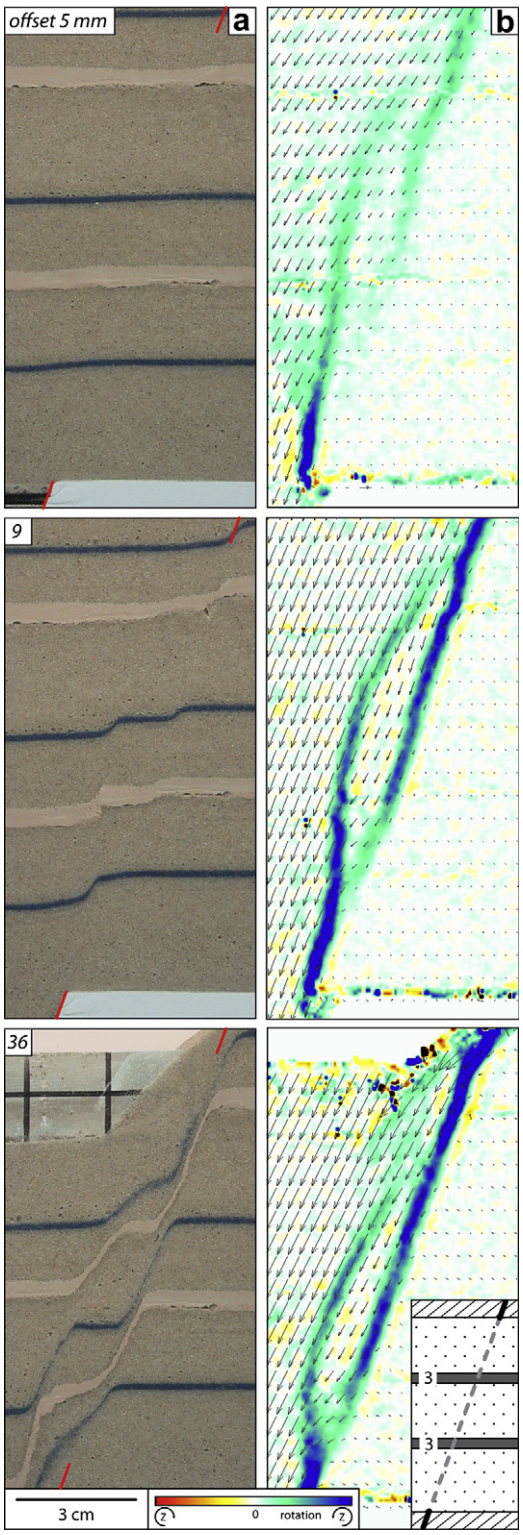

Fig. 8. (a) Image sequence showing experiment C2-4-s-tp with two 3 mm thick cemented clay layers and top plates (see inset). Basement fault offset is 5, 9 and 36 mm. Red lines indicate location of rigid blocks at bottom and top. (b) Image sequence showing the corresponding PIV overlay to the image sequence in (a) with the velocity vector field in the foreground and a contour plot of the z-component of the incremental rotation field in the background. (For interpretation of the references to colour in this figure legend, the reader is referred to the web version of this article.)

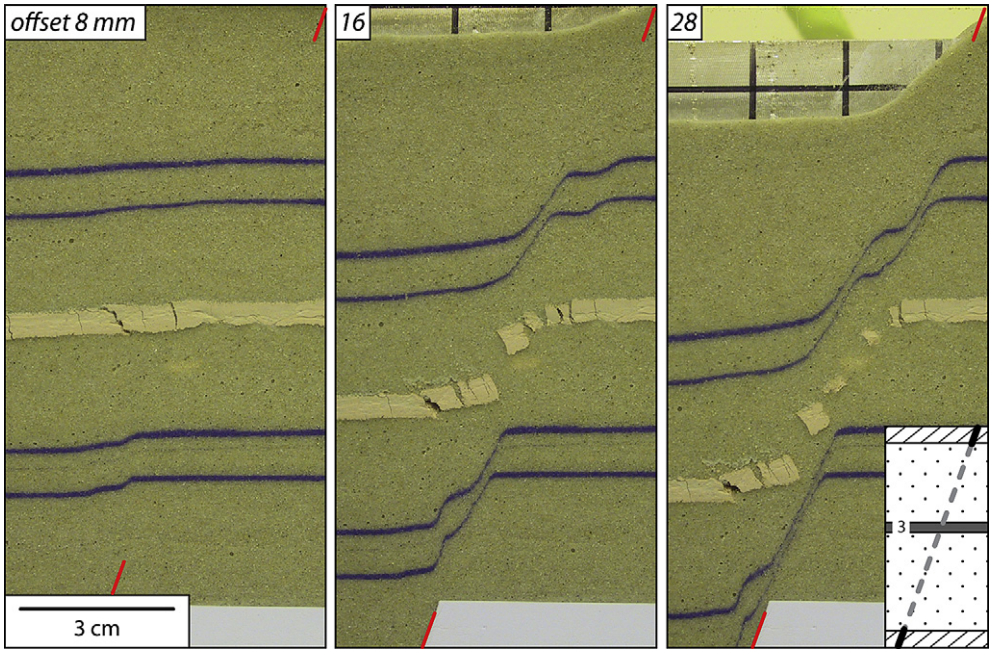

Fig. 9. Image sequence showing experiment C1-6-s-tp with one 3 mm thick cemented clay layer and top plates (see inset). Basement fault offset is 8, 16 and 28 mm. Red lines indicate location of rigid blocks at bottom and top. (For interpretation of the references to colour in this figure legend, the reader is referred to the web version of this article.)

soft clay to 0.25 kPa for soft clay with 0.25 wt.% cement). We observe two precursor faults initiating from the basement and from the top. The lower fault initiates with a steep dip, but, after intersecting the lower clay layer, it curves towards the footwall. The upper fault evolves in its kinematically favored plane. Both faults are active throughout the experiment, with a progressively thinning but stable fault lens between the two active fault strands (Fig. 8b). Continuous clay smear forms everywhere in the model. The two experiments described above are therefore similar initially, but the second experiment allows simultaneous displacement on two fault surfaces whereas the first experiment constrained displacement to one fault strand.

3.2.2. *High competence contrast*

3.2.2.1. Strong clay. Experiment C1-6-s-tp (Fig. 9, Table 1) contains a single, 3 mm thick clay layer 60 mm above the basement. The clay contains 10 wt.% cement and is cured only partly, so its strength is approximately the same as the completely cured, 2 wt.% cemented

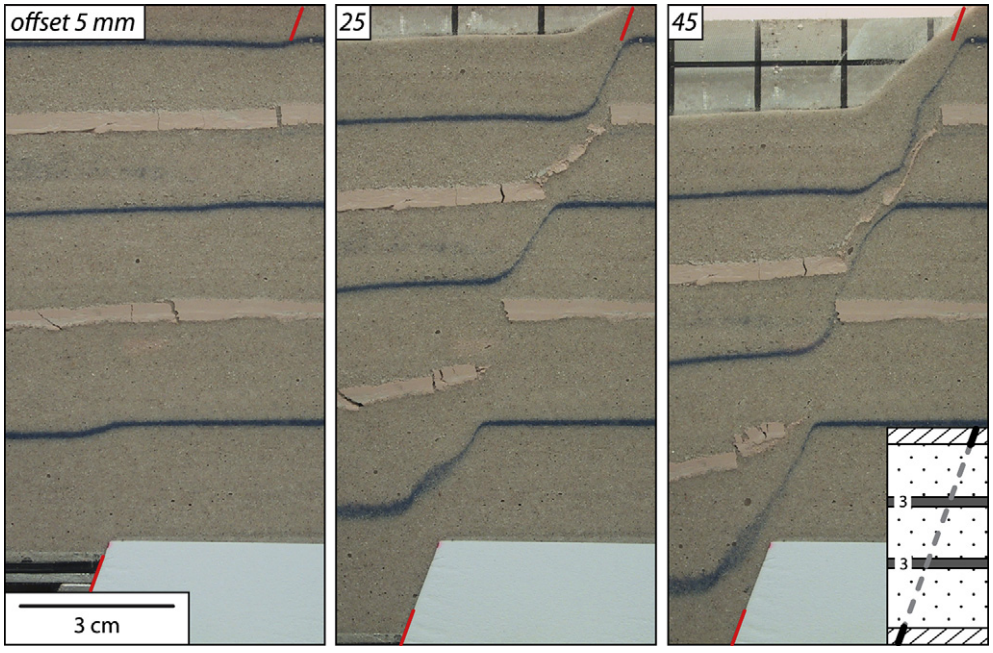

Fig. 10. Image sequence showing experiment C2-3-s-tp with two cemented (1.5 wt.%) clay layers and top plates (see inset). Basement fault offset is 5, 25, and 45 mm. Red lines indicate location of rigid blocks at bottom and top. (Transparent, reddish box in center of photos is a camera reflection). (For interpretation of the references to colour in this figure legend, the reader is referred to the web version of this article.)

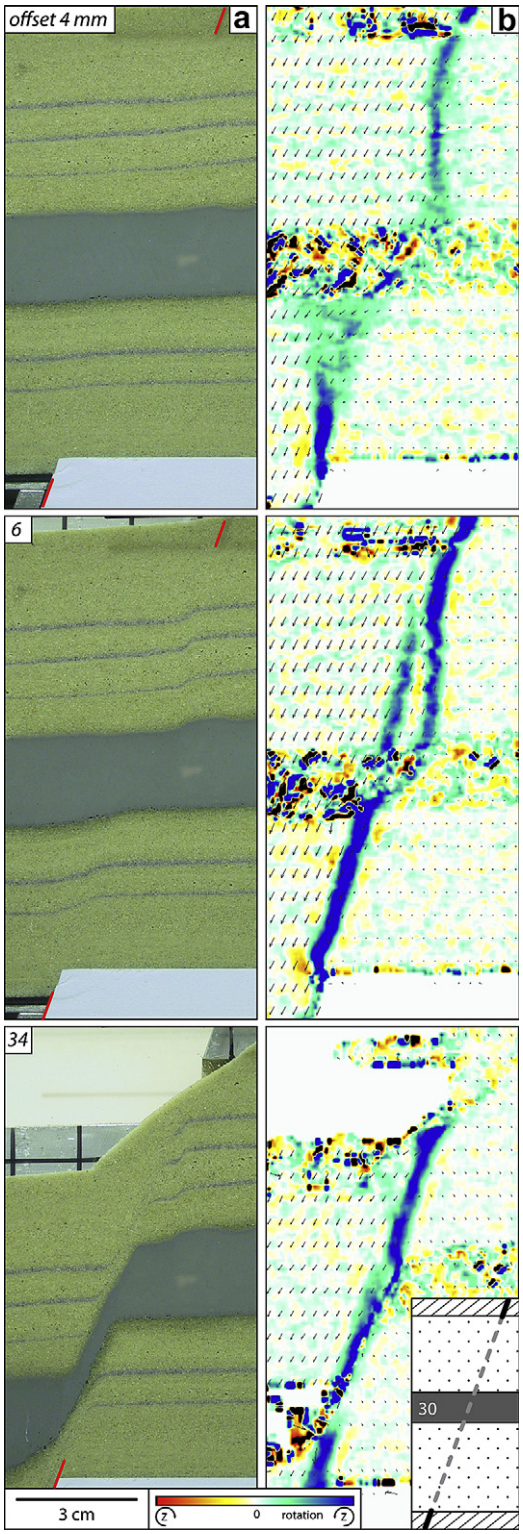

Fig. 11. (a) Image sequence showing experiment N-2-s-tp with one 30 mm thick soft-clay layer (see inset) and top plates. Fault offset is 4, 6 and 34 mm. Approximate fault location is traced with red lines. (b) Image sequence showing the corresponding PIV overlay to the image sequence in (a) with the contour plot of incremental rotation field and the velocity vector field. (For interpretation of the references to colour in this figure legend, the reader is referred to the web version of this article.)

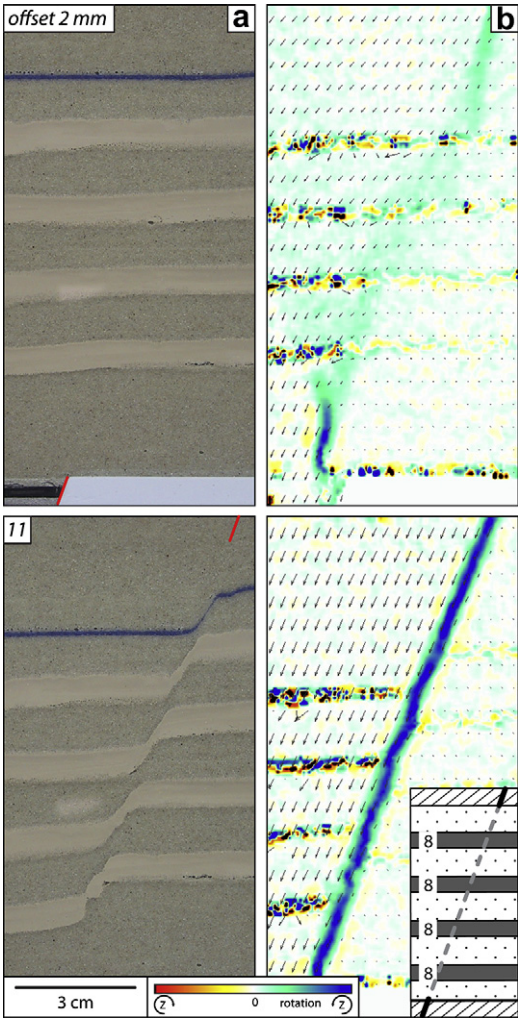

Fig. 12. (a) Image sequence showing experiment experiment M-1-s-tp with four 8 mm thick soft-clay layers and top plates (see inset). Fault offset is 2 and 11 mm. Red lines indicate location of rigid blocks at bottom and top. Fig. 17 shows final stage of this experiment. (b) Image sequence showing the corresponding PIV overlay to the image sequence with the contour plot of incremental rotation field and the velocity vector field. (For interpretation of the references to colour in this figure legend, the reader is referred to the web version of this article.)

clay. Deformation involves monoclinal bending of the clay followed by fracturing and block rotation. The shear zones in the sand form a wide lens with continuous activity on multiple fault strands. The interior of the lens is highly deformed, in contrast to the previously described experiments.

Experiment C2-3-s-tp (Fig. 10, Table 1) has two layers of 3 mm thick clay. The clay was fully cured but with only 1.5 wt.% cement. As in the previous experiment, initial deformation causes brittle failure in both layers. Progressive deformation leads not only to displacement and rotation of the fragments, but also to progressive erosion of the fragment edges, forming a ductile clay gouge with clay clasts and core–mantle structure around the old fragments.

3.2.2.2. Weak clay. Experiment N-2-s-tp contains one 30 mm thick, soft-clay layer (Fig. 11, Table 1). A near-vertical precursor fault initiates from the basement fault tip. After 2 mm displacement on the basement fault, deformation localizes at the tip of the fault between the top plates and propagates downward. With progressive deformation these two zones interact and overlap, forming a restraining relay zone across the clay layer (Fig. 11a, center). Initial

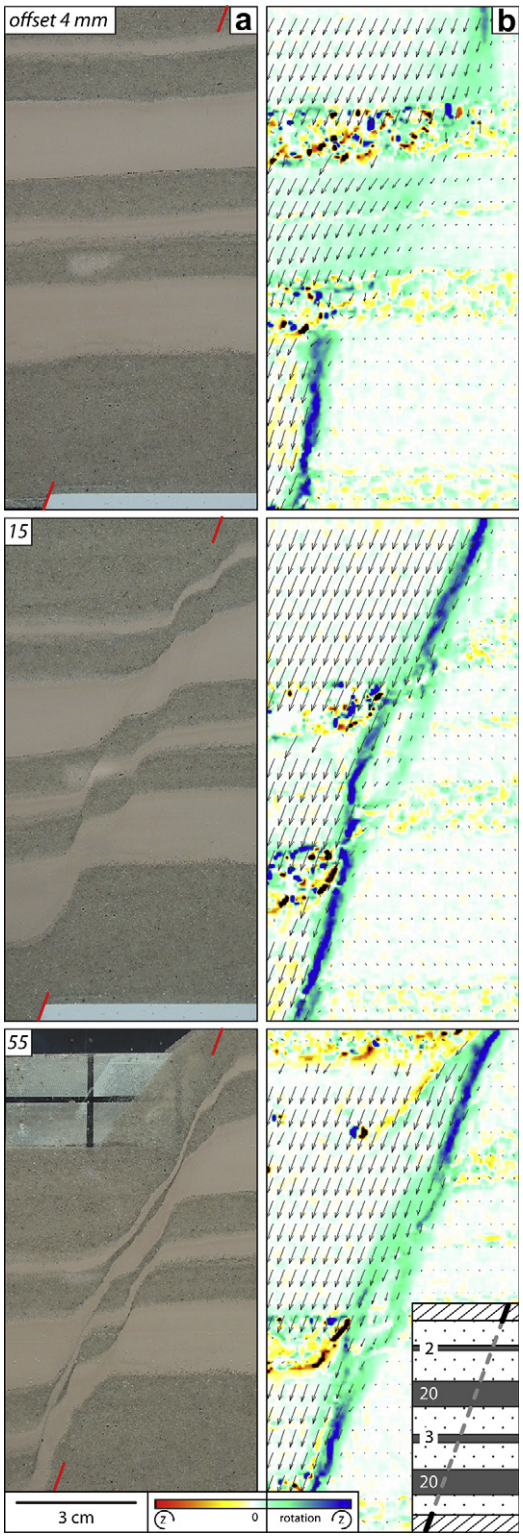

Fig. 13. (a) Image sequence showing experiment M-2-s-tp with four soft-clay layers and top plates (see inset). Basement fault offset is 4, 15 and 55 mm. Red lines indicate location of rigid blocks at bottom and top. (b) Image sequence showing the corresponding PIV overlay to the image sequence in (a) with the contour plot of incremental rotation field and the velocity vector field. (For interpretation of the references to colour in this figure legend, the reader is referred to the web version of this article.)

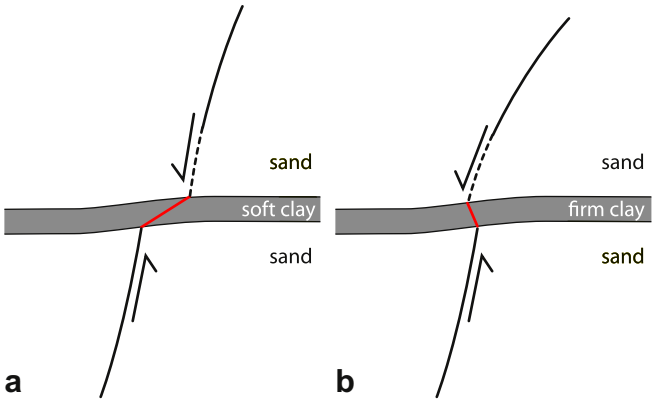

Fig. 14. Sketch of the first-order differences in kinematics between experiments containing soft (a) and firm (b) clay layers.

deformation in the clay layer is in this restraining zone (cf. Egholm et al., 2008). With increasing displacement, the top precursor fault becomes inactive, and deformation switches to a new strand forming a restraining relay zone relative to the fault below the clay layer (Fig. 11b, bottom). At the same time, the fault below the clay layer rotates clockwise, producing a gentle curving geometry at the lower sand–clay contact that is similar to normal-drag folds. This fault evolution produces a stable, planar deformation zone with an unusually thick clay gouge.

3.2.3. *Effect of multiple layers and layer thickness*

Experiment M-1-s-tp has four 12 mm thick soft-clay layers alternating with 8 mm thick sand layers (Fig. 12, Table 1). The fault-zone evolution in this experiment is similar to the reference experiment with only sand (Fig. 4). The initially steep precursor faults form a restraining zone across the sand–clay sequence with minor fault segmentation. Deformation in this sequence evolves into the kinematically favored plane. Each clay layer forms a continuous clay smear in the layered gouge, but the sand between the clay layers thins and in some cases becomes boudinaged (Fig. 12). A similar setup with four soft clay layers but variable layer thickness (Fig. 13, Table 1, experiment M-2-s-tp) illustrates the effect of layer thickness on fault-zone evolution. Here, the total thickness of the clay-rich interval is more than in the previous experiment (75 vs. 62 mm), and the clay–sand ratio is also higher (3:2 vs. 2:3). The two initially steeply dipping precursor faults connect in a zone of diffuse deformation with a shallower dip than the initial segments. Localization of deformation occurs on both sides of this zone with a less deformed lens in between. With progressive deformation the sheared sand in the fault zone becomes discontinuous as individual, sheared clay layers coalesce.

4. Discussion

4.1. *Effect of boundary conditions on fault-zone evolution*

Faults in nature form under a variety of local boundary conditions, but in many cases those boundary conditions might be less than those imposed here (Schmatz et al., 2010). In this study we explored normal fault development in weak materials layered between two rigid layers faulted with the same 70° dip and lying in the same plane. The resulting fault evolution differs dramatically from experiments with a rigid lower boundary condition and a free upper surface.

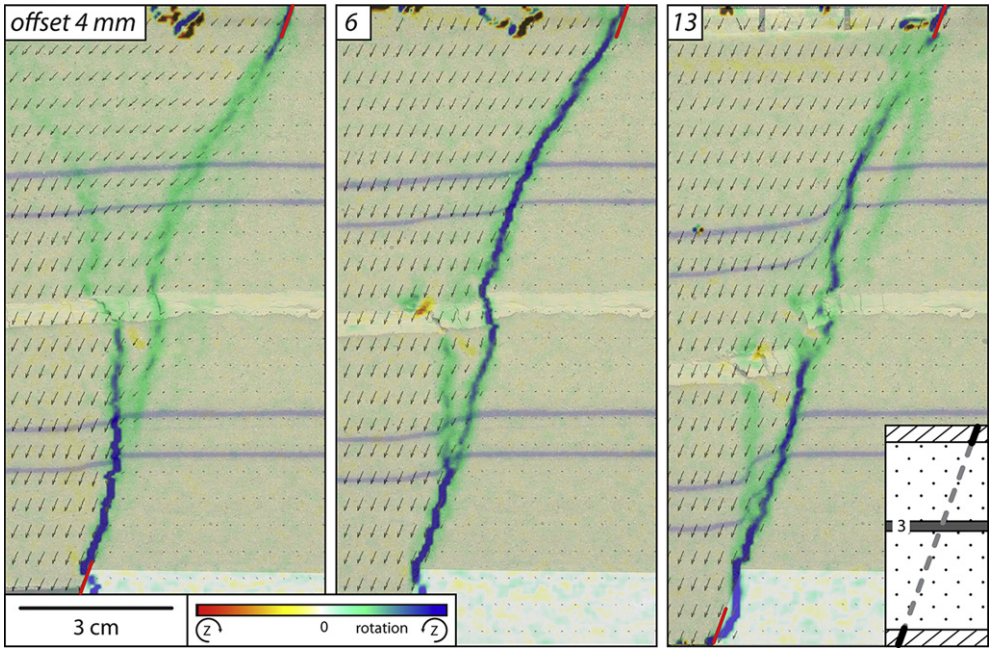

Fig. 15. PIV analysis of the experiment in Fig. 10, showing the formation of asperities and lens structures. Basement fault offset is 4, 6 and 13 mm. Red lines indicate location of rigid blocks at bottom and top. (For interpretation of the references to colour in this figure legend, the reader is referred to the web version of this article.)

Imposing the rigid, faulted top boundary strongly controlled the geometry of the resulting shear zone, producing kinematics similar to those in a direct shear experiment (Zhang and Thornton, 2007). Using geotechnical nomenclature, our setup is defined as a "slanted direct shear" experiment. Post-mortem excavation of the fault zones revealed few edge effects due to frictional drag along the glass panels on the evolution of faults (Souloumiac et al., 2009), but further study is ongoing.

As expected from previous work, the first localization of deformation along precursor faults started at the intersection of the faults in the basement and top blocks. The position of these initial faults is controlled by the stress fields around the fault tips, and they rotate either continuously or in steps into the kinematically favorable plane defined by the basement and top fault plane. In our earlier experiments with a free top surface, this effect was only present in the bottom part of the model. To some degree, the experiments with the top blocks represent a symmetrical doubling of the free-surface experiments. Localization from the top fault is delayed from the initial basement offset as stresses propagate from the basement upward. The kinematics of our experiments in some cases resemble the Quadshear model (Welch et al., 2009) in which a ductile interval sandwiched between two brittle layers becomes sheared, although these models are purely kinematic and contain no mechanical properties.

Reproduction of experiments with and without a top-plate boundary condition (Figs. 3 and 5) reveals that the top plate suppresses but fails to eliminate initial fault branching. The top plate results in less segmentation and a less complex fault zone in general (Childs et al., 1996; Van der Zee and Urai, 2005). A single, planar fault zone forms earlier in the experiment when a top plate is present, but the continuous history of deformation during early displacement seems significant to us, even though it is abbreviated with the top plate. The folding that arises from the migration of a shear surface appears similar to a normal-drag fold, but its formation is different than the processes expected when a single, planar fault propagates into a thick, layered sequence, such as the slightly downwards-widening shear zone in Fig. 4.

4.2. Competence contrast

In our models, normal faulting starts from the tip of a preexisting fault in a competent brittle bed (basement) where the overlying layers accommodate a certain amount of strain (Mandl, 2000). In experiments with soft and normally consolidated clay, the strain is continuous without the formation of fractures, at least at the scale of observation. In all cases, this produces continuous smear along the fault surface in our 2D sections along the glass plate. These observations agree with earlier studies by Sperrevik et al. (2000) and Van der Zee and Urai (2005). Clay containing a small amount of Portland cement (0.25 wt.% in soft clay) deforms in this same manner because the increase in strength is insignificant compared to the mean effective stress (van Gent et al., in press). Even normal clay layers up to 10 mm thick have minimal effect on initial fault localization, which we interpret to result from the low competence contrast between sand and clay. In experiments with a thick, soft-clay layer (Figs. 11 and 13) the initial faults are longer-lived, leading to the formation of a restraining step in the clay layer that progressively thins out (Fig. 14). The clay in the restraining step is strongly deformed until a new fault forms with a releasing geometry, forming a final, thick clay gouge. This structure is similar to that in Fig. 10 of Van der Zee and Urai (2005) for which a similar kinematic evolution was proposed. The early evolution is also consistent with the DEM results of Egholm et al. (2008), although no evidence of the overstepping process is presented. A full mechanical explanation of the parameters that control this "overstepping" is the aim of an ongoing study using numerical and experimental methods.

In experiments with very hard clay (firm, over-consolidated clay or cemented clay), the fault-zone geometry is affected by fractures in the clay that form in areas of high curvature as the layers are bent (Figs. 9 and 10). In this case, a releasing relay zone forms between the two faults propagating from the tips of the faults in the top and bottom blocks (Fig. 14). This result compares with models by Mandl (2000) and Lehner and Pilaar (1997) in which initial monoclinal bending of the clay is interpreted to have changed the orientation

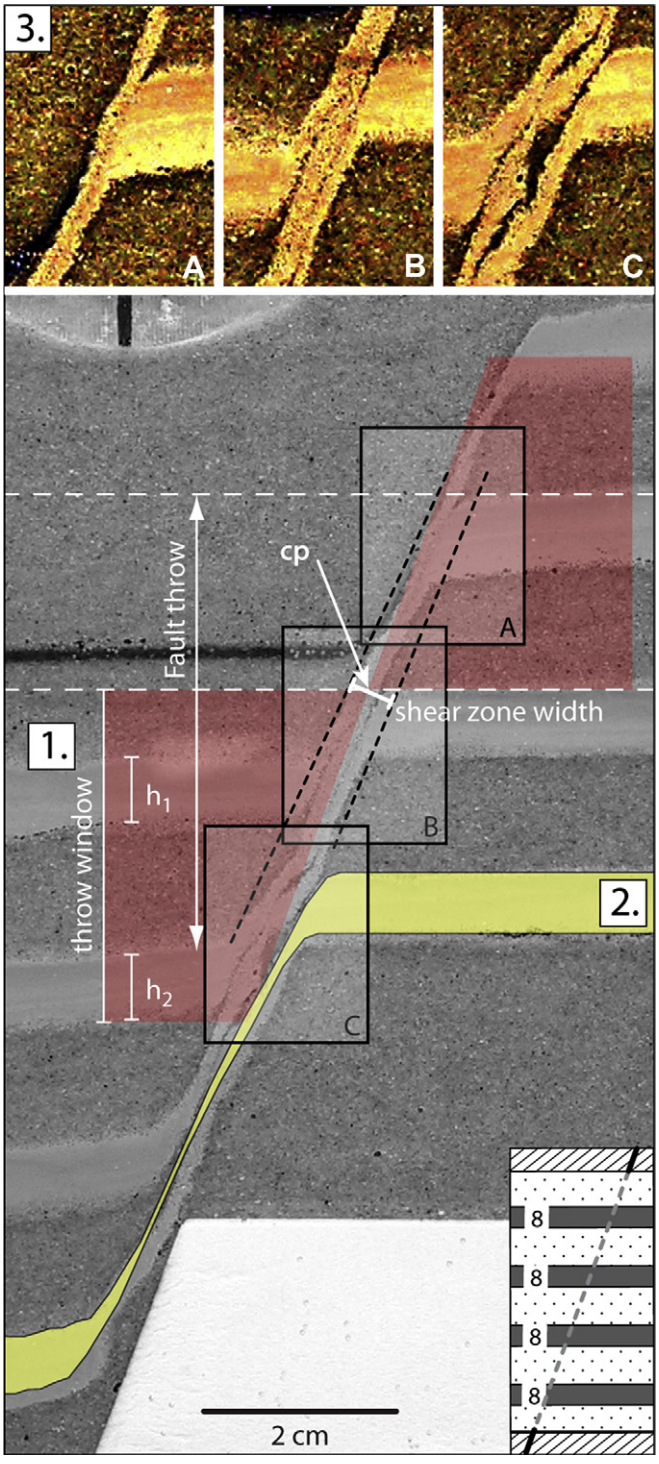

Fig. 16. Photograph of experiment M-1-s-tp showing: 1) The SGR measuring method after Fristad et al. (1997) applied to our experiments, with calculation point cp. SGR = ∑shale bed thickness (h)/fault throw × 100% (31% in this example); gouge clay = ∑clay band thickness/shear zone width × 100% (62% in this example); 2) a simple-shear overlay on the lowermost clay layer indicating the accumulation of clay in the shear zone; and 3) three selected areas of the fault zone enhanced to increase contrast. The original clay layer shows much less variance in color than the material in the fault zone, and where the color variance is proportional to the grain size of the sand (wavelength). This is interpreted to be a result of a mixture of sand and clay in the fault zone. (For interpretation of the references to colour in this figure legend, the reader is referred to the web version of this article.)

and magnitude of the principal stresses. Changes in the stress tensor allow the formation of secondary slip planes that cause internal segmentation of the clay layer. Schöpfer et al. (2006) investigated the deformation of multilayers under similar boundary conditions using DEM techniques in materials where the strong layers undergo tensile failure and the weaker layers deform by faulting. They observed that, after the formation of monoclines, the fault zone propagates in a staircase-like manner, with vertical tensile fractures in the strong layers connected by shear fractures in a complex fault zone. Although the details of the material properties are quite different, their results are best compared with our results of cemented clay layers. The striking difference is that, in our case, each strong layer develops two fractures, one in the plane of the principal fault and the other along the plane of the initial precursor fault. In the models of Schöpfer et al. (2006), most layers initially develop only one fracture, but a second fracture develops in the layer closest to the stiff basal layer, followed by block rotation of a clay fragment, similar to the observations in our experiments.

In field observations of normal faults by Van der Zee et al. (2008), tensile fractures in the brittle layers are also attributed to the evolution of the fault zone. In this case, however, the fractures are interpreted to have formed before faulting and in different orientations than the fault, adding additional geometric complexity.

One additional, important process is the reworking of brittle clay fragments in the fault zone (Lindsay et al., 1993; Holland et al., 2006, and others). In our experiments (Fig. 10), reworking requires no more than a modest competence contrast between sand and clay because of the relatively small displacements. Because abrasion is an irreversible process, we expect this process becomes more important for faults with larger displacements (i.e. 10s of meters).

4.3. Lens formation

Branches in fault zones defining a lens (or horse) are commonly observed in both nature and experimental studies (Ramsay and Huber, 1987; Childs et al., 1996, 1997; Walsh et al., 1999; Van der Zee and Urai, 2005; Lindanger et al., 2007). In addition to fault lenses caused by segment linkage, we observe lenses that formed by asperity bifurcation (Lindanger et al., 2007). The formation of asperities is common in most firm clay and cemented clay experiments. As shown in Fig. 15 (experiment in Fig. 9, Table 1, experiment C1-6-s-tp), these lenses evolve considerably through time. Asperities are eroded progressively while continued localization causes the formation of new asperities. Asperity-related lenses may thin and tighten while new lenses are forming. The model of Van der Zee (2002) suggests that material inside the lens becomes more strongly deformed than the surrounding rock. The formation of fault-bounded lens structures in our experiments is related to the initial pattern of localization and the evolution of segmentation. In experiment C2-4-s-tp (Fig. 8, Table 1), a wide lens develops after coalescence of the initial zones of localization. Although the lens becomes eroded by deformation, its interior remains undisturbed as indicated by PIV (Fig. 8b). Clearly, the evolution of deformation in fault-bounded lens structures is more complicated than suggested by the models of Van der Zee and Urai (2005) and Lindager et al. (2007).

4.4. Clay smear

According to Fulljames et al. (1997), the amount of clay smear at a point on the fault reduces with distance to the source bed. In their interpretation the smear forms a layered gouge containing clay from each source bed: the greater the number and thickness of the source beds, within the throw window, the greater the thickness of

the smear. Lindsay et al. (1993) distinguished among three types of clay smear: (i) abrasion due to movement past sandstones, (ii) shearing and ductile deformation between hanging wall and footwall cut-offs of shale beds, and (iii) injection of clays during fluidization. Our experiments show that clay smear in the form of a continuous clay band on the fault surface is caused by fault segmentation followed by shearing (e.g. Figs. 7, 12 and 13). Asperity abrasion and reworking of the clay also contribute to the formation of clay smear (Fig. 10). Clausen and Gabrielsen (2002) investigated clay smear processes with the help of a ring-shear apparatus and concluded that the potential for developing a continuous clay membrane increases as: (1) the normal stress increases, (2) the water content of clay increases, and (3) the shear strength of clay decreases. Our results are in agreement with these three inferences. (1) Addition of the top plate causes continuous clay smear in a model where clay fractures and becomes discontinuous without the top plate. Although in these two experiments (Figs. 5 and 6) the vertical stress at the top of the clay layer is the same, the presence of the stiff aluminum plate, which resists bending, acts to increase the mean stress in the region of the fault zone. (2) All soft-clay experiments show continuous clay membranes. (3) Measurements of shear strength (Schmatz et al., 2010) show the lowest shear strength for soft clay.

4.5. Shale-gouge ratio (SGR)

The SGR method estimates the proportion of clay incorporated into the fault gouge as a function of the sand/shale ratio which moved past a point on a fault (Crawford et al., 2002). The shale thicknesses are measured in a window with a height equal to the throw (e.g., Yielding et al., 1997). We calculated SGR according to this algorithm (Figs. 16 and 17) in each of the experiments in Table 1. The amount of gouge clay in the fault zone is defined as the clay thickness as a percentage of the total shear zone thickness as defined in PIV analyses (Fig. 16). SGR plotted against gouge clay in the fault zone for most of our experiments (Table 1) illustrate that there is no simple correlation between the two parameters (Fig. 17), and in most cases there is either more or less clay in the fault than expected from an SGR calculation. Normally consolidated clay is both enriched and depleted in the fault. Soft clay leads to more clay within the gouge zone than expected from SGR (for 79% of the cases there is more clay in the fault than expected from SGR). Brittle clay tends to be depleted, albeit with a large scatter (in 85% of the experiments, there is less – and commonly far less – clay in the fault zone than expected from SGR). However, SGR yields only an average of the amount of clay expected within the fault zone (Van der Zee and Urai, 2005) and if all clay types are present, the average SGR value will result. However, in settings where one clay type dominates, there may be significant bias in the calculated SGR value. Moreover, the experiments illustrate large local variability around the calculated SGR value within a consistent throw window.

4.6. Mixing

Fault zones typically exhibit heterogeneous, non-coaxial deformation (Mair and Abe, 2008). In the case of simple shear, the geometry of clay or sand within the fault zone is derived from the fault-zone width, the original layer thickness, and the fault angle. A simple-shear overlay on the final gouge zone of experiment M-1-s-tp (Fig. 16) shows that clay-gouge zone is thicker than expected from simple shear, although there is no evidence of lateral clay injection from the source layer (Van der Zee et al., 2003). One process that contributes more clay to fault gouge than expected from simple shear is mechanical mixing, in which clay moves into the porosity of the sheared sand (Van der Zee, 2002). Clausen and Gabrielsen (2002) reported three stages in the development of clay membranes from ring-shear experiments. In their first stage corresponding to low normal stress (6 kPa), clay membranes are completely absent. Only occasional clay fragments occur in the fault zone. In the second stage at higher normal stress (>25 kPa), a mixture of sand and clay or patches of clay embedded in a sand matrix occur. In the third stage, a semi-continuous clay membrane develops (normal stress > 100 kPa). They inferred that parts of the fault zone characterized by a clay–sand mixture are stable and develop no other types of smear. They also speculated that mixing of clay and sand occurs by local invasion of clay into sand pores generated in dilation at an early stage of shear under low normal stress. Clausen and Gabrielsen (2002) concluded that, after rupture of the clay layers, the fault zone is dominated by plastic deformational processes, which include transport of single grains from sand into the clay. Crawford et al. (2002) also reported on the generation of anastomosing networks of microsmears around framework grains or clasts. In our experiments mixtures of sand and clay within the gouge zone are also present. A detailed investigation of digitally enhanced high-resolution digital images (Fig. 16, experiment M-1-s-tp) shows that clay in the shear zone differs in composition from the undeformed source clay. A fault gouge consisting of sand, clay and sand–clay mixture replaces the initial sheared layers of sand and clay.

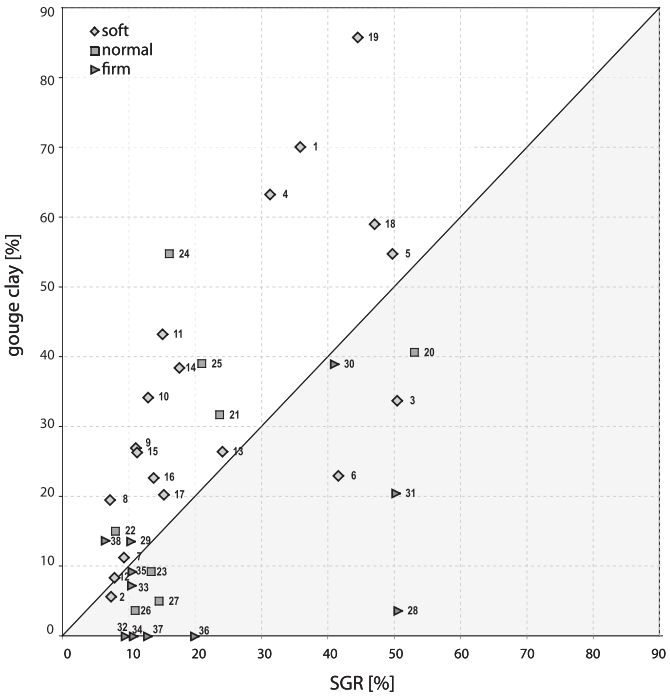

Fig. 17. Graph of SGR measured in all experiments (numbers refer to experiment number in Table 1) plotted against the percentage of clay (gouge clay) in the fault zone.

4.7. Incipient faulting

Understanding localization in the layered sand–clay experiments requires a clear understanding of localization in a pure sand experiment. Assuming that the initial deformation in our models is non-localized, we sought evidence for this with PIV. We carefully processed the results of the first few photographs of a number of experiments, plotting the velocity field for basement fault displacements up to 0.8 mm (Fig. 18). In the first example we show the incremental displacement vector field in the lower 6 cm of a sand-only experiment (Fig. 4). Here, there is initially a concentric

vector field centered on the tip of the basement fault, as predicted in the analytical models of Patton and Fletcher (1995) for an elastic material. Ongoing deformation makes the vector field much more discontinuous, reflecting the initial localization of strain. Experiment N-2-s-tp (Fig. 11) shows a similar early evolution. The semi-concentric vector field is observed in the initial phase, but with some decoupling across the clay layer. With ongoing deformation, localization is much more rapid in the sand below the soft-clay layer.

4.8. Application to fault zones in nature

The results of our experiments simulate the formation of cm-scale faults in saturated sand–clay sequences with minimal overburden under very specific boundary conditions and therefore, extrapolation to fault-zone evolution in layered sequences in nature is complicated. True scaling would require knowledge of model-to-nature ratios of length, density, gravity, and cohesion; however, in nature these parameters exhibit a wide range of values. Upscaling to faults cutting lithified sequences is even more problematic because, at this scale, the fault-zone widths (controlled by the size of the sand grains) will likely be much larger than for upscaled faults.

Nonetheless our experiments qualitatively compare with nature when only minor length upscaling is required, such as for small faults in thinly bedded sand–clay sequences like those described in Van der Zee and Urai (2005) (Fig. 19; see full description in caption). Here, many of the structures in our multilayers (Figs. 12 and 13, cf. Figs. 6, 9, 10, 14 of Van der Zee and Urai, 2005) are similar, suggesting that the differences in mechanical properties play a relatively minor role in controlling the evolution. Considering constitutive properties, for both soft and hard clay end-members embedded in sand, the patterns of deformation are quite distinct, and seem to be reasonably consistent, in experiment and in numerical simulation (Mair and Abe, 2008; Schöpfer et al., 2006; Egholm et al., 2008). This suggests that these patterns are independent of small variations in material properties and are therefore reasonably robust and might be expected in nature, too.

The effect of different boundary conditions on how the structures evolved is the most difficult to evaluate based on our results. The initially segmented nature of normal faults has been extensively documented, and Van der Zee et al. (2003) suggested that it is in the segment links where the presence of soft or hard clay layers causes the strongest deviations from a simple deformation band. Results of this study show, in agreement with earlier work (e.g. Childs et al., 1996; Schöpfer et al., 2006; Egholm et al., 2008), that the presence of a mechanical stratigraphy has a strong control on the location of segment linkage. However, the change in importance of the precursor faults with increasing burial and length scale is unclear and requires additional study.

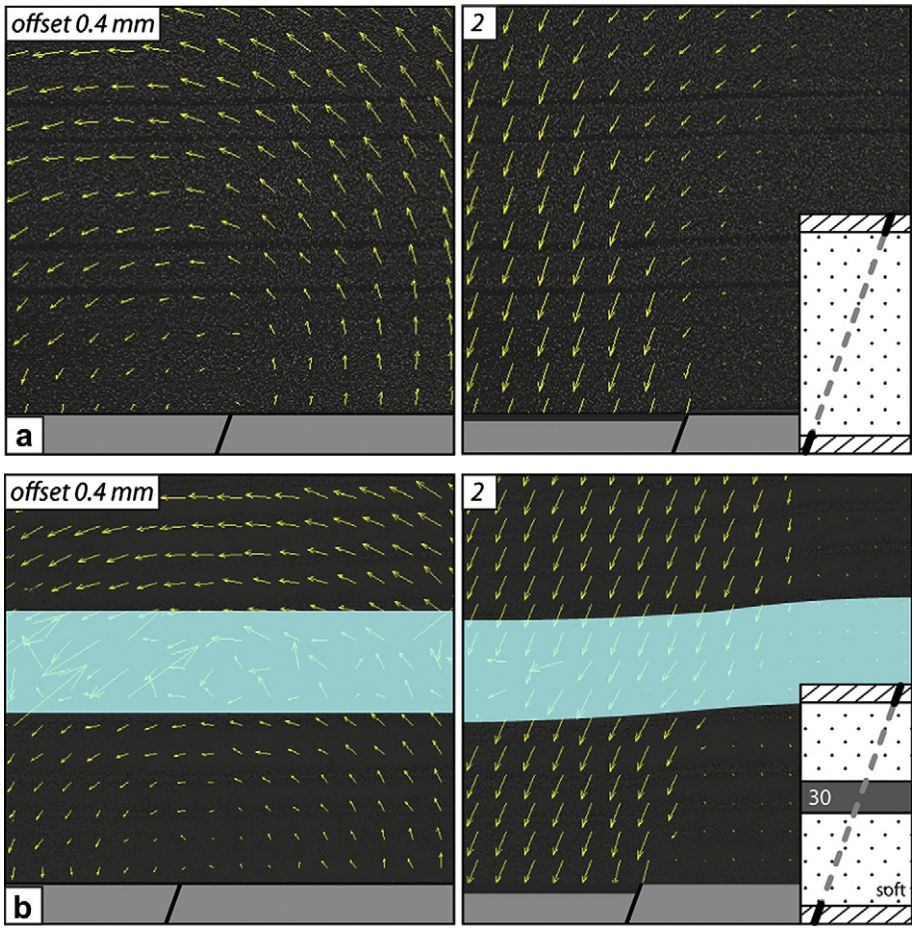

Fig. 18. Images showing the incremental vector field of the initial stages of experiments with top plates: (a) experiment P-2-tp and (b) experiment N-2-s-tp (a 30 mm thick soft-clay layer), with the point of observation at the tip of the basement fault. The vector fields are for basement fault offsets of 0.4 and 2 mm. The vector field for the clay layer is invalid and covered with a transparent, blue mask. (For interpretation of the references to colour in this figure legend, the reader is referred to the web version of this article.)

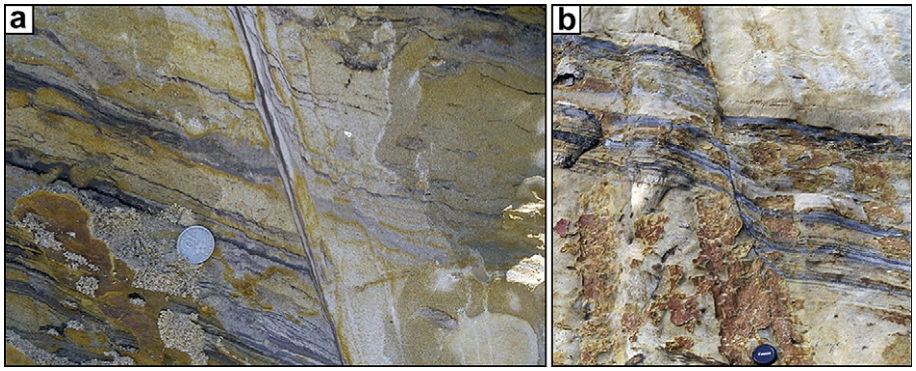

Fig. 19. Field examples of normal faults formed at approximately 800 m in a deltaic sand–clay sequence near Miri, Sarawak, Malaysia. (a) Complex clay-rich gouge in a fault with an offset of 2.5 m. The sheared clay and sand develops into a banded fault gouge; coin for scale. (b) Small-offset fault in thinly layered sand and clay with thin clay gouge (lens cap for scale). See Van der Zee and Urai (2005) for further information.

5. Conclusions

1. The mechanical properties of clay have a major effect on clay-gouge evolution during fault-zone development in sand–clay sequences.
2. The structure of initially localized deformation evolves into a kinematically favorable fault-zone structure. This evolution has a major role in controlling fault-zone structures (e.g., releasing and restraining relay zones).
3. A high competence contrast between sand and clay leads to a more complex fault zone due to the formation of secondary localized zones and segmentation-induced fault lenses. A high competence contrast also promotes coeval strain partitioning between multiple shear zones.
4. Weak clay layers are preferentially enriched in normal fault zones, whereas strong, brittle clay initially fractures and forms clay boudins that rotate in the deforming sand. With progressive deformation these boudins are abraded and transformed into a soft-clay gouge.
5. Empirical methods such as SGR used to predict fault seal can be improved by taking into account the mechanical properties of the faulted rocks.
6. The low permeability clay gouge thickens with fault displacement due to mixing of sand and clay.

Acknowledgements

This research would not be in its present state without the contributions of a number of persons. In particular the authors would like to thank M. Holland, S. Giese, M. Ziegler, W. van der Zee, J. Wilden and K. Nienhaus. B. Maillot, A. Henza and especially R. Schlische are acknowledged for their constructive reviews and editorial help. This work was funded by ExxonMobil and, as part of the ongoing research project UR 64/10-1, is supported by the German Science Foundation DFG.

References

Adam, J., Urai, J.L., Wieneke, B., Oncken, O., Pfeiffer, K., Kukowski, N., Lohrmann, J., Hoth, S., van der Zee, W., Schmatz, J., 2005. Shear localisation and strain distribution during tectonic faulting-new insights from granular-flow experiments and high-resolution optical image correlation techniques. Journal of Structural Geology 27, 283–301.

Antonellini, M.A., Aydin, A., Pollard, D.D., 1994. Microstructure of deformation bands in porous sandstones at Arches National Park, Utah. Journal of Structural Geology 16, 941–959.

Cardozo, N., Bhalla, K., Zehnder, A.T., Allmendinger, R.W., 2003. Mechanical models of fault propagation folds and comparison to the trishear kinematic model. Journal of Structural 25, 1–18.

Childs, C., Nicol, A., Walsh, J.J., Watterson, J., 1996. Growth of vertically segmented normal faults. Journal of Structural Geology 18, 1389–1397.

Childs, C., Walsh, J.J., Watterson, J., Møller-Pedersen, P., 1997. Complexity in fault zone structure and implications for fault seal prediction. In: Møller–Pedersen, P., Koester, A.G. (Eds.), Hydrocarbon Seals. NPF special publication 7. Elsevier, Amsterdam, pp. 61–72.

Clausen, J.A., Gabrielsen, R.H., 2002. Parameters that control the development of clay smear at low stress states: an experimental study using ring-shear apparatus. Journal of Structural Geology 24, 1569–1586.

Crawford, B.R., Myers, R.D., Woronow, A., Faulkner, D.R., Rutter, E.H., 2002. Porosity–Permeability Relationships in Clay-bearing Fault Gouge. Society of Petroleum Engineers, Irwing, Texas, 78214, pp. 13.

Egholm, D.G., Clausen, O.R., Sandiford, M., Kristensen, M.B., Korstgård, J.A., 2008. The mechanics of clay smearing along faults. Geology 36, 787–790.

Erslev, E.A., 1991. Trishear fault-propagation folding. Geology 19, 617–620.

Ferrill, D.A., Morris, A.P., 2003. Dilational normal faults. Journal of Structural Geology 25, 183–196.

Fristad, T., Groth, A., Yielding, G., Freeman, B., 1997. Quantitative fault seal prediction: a case study from Oseberg Syd. In: Møller–Pedersen, P., Koester, A.G. (Eds.), Hydrocarbon Seals. NPF special publication 7. Elsevier, Amsterdam, pp. 107–124.

Fulljames, J.R., Zijerveld, L.J.J., Franssen, R.C.M.W., 1997. Fault seal processes: systematic analysis of fault seals over geological and production time scales. In: Moeller-Pedersen, Koester, A.G. (Eds.), Hydrocarbon Seals. NPF special publication 7. Elsevier, Amsterdam, pp. 51–59.

van Gent, H.W., Holland, M., Urai, J.L., Loosveld, R., Evolution of fault zones in carbonates with mechanical stratigraphy – insights from scale models using layered cohesive powder. Journal of Structural Geology: Special publication., in press.

Holland, M., Urai, J.L., van der Zee, W., Stanjek, H., Konstanty, J., 2006. Fault gouge evolution in highly overconsolidated claystones. Journal of Structural Geology 28, 323–332.

Horsfield, W.T., 1977. An experimental approach to basement-controlled faulting. Geologie en Mijnbouw 56, 363–370.

James, W.R., Fairchild, L.H., Nakayama, G.P., Hippler, S.J., Vrolijk, P.J., 2004. Fault-seal analysis using a stochatic multifault approach. AAPG Bulletin 88, 885–904.

Lehner, F.K., Pilaar, W.F., 1991. On a mechanism of clay smear-emplacement in-synsedimentary normal faults (abstract). AAPG Bulletin 75, 619.

Lehner, F.K., Pilaar, W.F., 1997. The emplacement of clay smears in synsedimentary normal faults: inference from field observations near Frechen, Germany. In: Moeller-Pedersen, Koester, A.G. (Eds.), Hydrocarbon Seals. NPF special publication 7. Elsevier, Amsterdam, pp. 39–50.

Lindanger, M., Gabrielsen, R.H., Braathen, A., 2007. Analysis of rock lenses in extensional faults. Norwegian Journal of Geology 87, 361–372.

Lindsay, N.G., Murphy, F.C., Walsh, J.J., Watterson, J., 1993. Outcrop studies of shale smears on fault surfaces. Special Publications. International Association of Sedimentologists 15, 113–123.

Mair, K., Abe, S., 2008. 3D numerical simulations of fault gouge evolution during shear: grain size reduction and strain localization. Earth and Planetary Science Letters 274, 72–81.

Mandl, G., 2000. Faulting in Brittle Rocks. Springer, London, pp. 434.

Patton, T.L., Fletcher, R.C., 1995. Mathematical block-motion model for deformation of a layer above a buried fault of arbitrary dip and sense of slip. Journal of Structural Geology 17, 1455–1472.

Peacock, D.C.P., Sanderson, D.J., 1992. Effects of layering and anisotropy on fault geometry. Journal of the Geological Society of London 149, 793–802.

Ramsay, J.G., Huber, M.I., 1987. The Techniques of Modern Structural Geology. In: Folds and Fractures, vol. 2. Academic Press, London, pp. 391.

Schmatz, J., Holland, M., Giese, S., van der Zee, W., Urai, J.L., 2010. Clay smear processes in mechanically layered sequences – results of water-saturated model experiments with free top surface. Journal of the Geological Society of India (special issue 03)

Schöpfer, M.P.J., Childs, C., Walsh, J.J., 2006. Localisation of normal faults in multilayer sequences. Journal of Structural Geology 28, 816–833.
Souloumiac, P., Leroy, Y.M., Maillot, B., Krabbenhøft, K., 2009. Predicting stress distributions in fold-and-thrust belts and accretionary wedges by optimization. Journal of Geophysical Research 114 B09404.
Sperrevik, S., Faerseth, R.B., Gabrielsen, R.H., 2000. Experiments on clay smear formation along faults. Petroleum Geoscience 62, 113–123.
Steingart, D.A., Evans, J.W., 2005. Measurements of granular flows in two-dimensional hoppers by particle image velocimetry. Part I: experimental method and results. Chemical Engineering Science 60, 589–598.
Urai, J.L., Nover, G., Zwach, C., Ondrak, R., Schöner, R., Kroos, B.M., 2008. Transport processes. In: Littke, R., Bayer, U., Gajewski, D., Nelskamp, S. (Eds.), Dynamics of complex intracontinental basins: The Central European Basin System. Springer, Berlin Heidelberg, pp. 367–388.
Van der Zee, W., 2002. Dynamics of fault gouge development in Layers sand–clay sequences. Shaker Verlag, Aachen, PhD thesis, pp. 155.
Van der Zee, W., Urai, J.L., Richard, P.D., 2003. Lateral clay injection into normal faults. GeoArabia 8, 501–522.
Van der Zee, W., Urai, J.L., 2005. Processes of normal fault evolution in a siliciclastic sequence: a case study from Miri, Sarawak, Malaysia. Journal of Structural Geology 27, 2281–2300.
Van der Zee, W., Wibberley, C.A.J., Urai, J.L., 2008. The influence of layering and preexisting joints on the development of internal structure in normal fault zones: the Lodeve basin, France. In: Wibberley, C.A.J., Kurz, W., Imber, J., Holdworth, R.E., Collerrini, C. (Eds.), The Internal Structure of Fault Zones: Implications for Mechanical and Fluid-Flow Properties. Geological Society of London Special Publications 299, pp. 57–74.
Walsh, J.J., Watterson, J., Bailey, W., Childs, C., 1999. Fault relays, bends and branchlines. Journal of Structural Geology 21, 1019–1026.
Weber, K.J., Mandl, G., Pilaar, W.F., Lehner, F.K., Precious, R.G., 1978. The role of faults in hydrocarbon migration and trapping in Nigerian growth fault structures. In: Proc. 10th Annual Offshore Technology Conference, Houston, Texas 4, 2643–2653.
Welch, M.J., Knipe, R.J., Souque, C., Davies, R.K., 2009. A Quadshear kinematic model for folding and clay smear development in fault zones. Tectonophysics, 186–202.
Wolf, H., Konig, D., Triantafyllidis, T., 2003. Experimental investigation of shear band patterns in granular material. Journal of Structural Geology 25, 1229–1240.
Yielding, G., 2002. Shale Gouge Ratio – calibration by geohistory. In: Koester, A.G.H.R. (Ed.), Hydrocarbon Seal Quantification. NPF Special Publication 11. Elsevier, Amsterdam, pp. 1–15.
Yielding, G., Freeman, B., Needham, D.T., 1997. Quantitative fault seal prediction. AAPG Bulletin 81, 897–917.
Zehnder, A.T., Allmendinger, R.W., 2000. Velocity field for the trishear model. Journal of Structural Geology 22, 1009–1014.
Zhang, L., Thornton, C., 2007. A numerical examination of the direct shear test. Geotechnique 57, 343–354.